


Symmetry-group-protected microfluidics

Jeremias Gonzalez , Ajay Gopinathan , and Bin Liu *

Department of Physics, University of California, Merced, California 95343, USA

 (Received 25 August 2023; revised 15 February 2024; accepted 22 April 2024; published 3 June 2024)

Modern micromanipulation techniques typically involve trapping using electromagnetic, acoustic, or flow fields that produce stresses on the trapped particles thereby precluding stress-free manipulations. Here, we show that by employing polyhedral symmetries in a multichannel microfluidic design, we can separate the tasks of displacing and trapping a particle into two distinct sets of flow operations, each characterized and protected by their unique groups of symmetries. By combining only the displacing uniform flow modes to entrain and move targeted particles in arbitrary directions, we were able to realize symmetry-protected, stress-free micromanipulation in 3D. Furthermore, we engineered complex, microscale paths by programming and controlling the flow within each channel in real time, resulting in multiple particles simultaneously following desired paths in the absence of any supervision or feedback. Our work therefore provides a general symmetry-group-based framework for understanding and engineering microfluidics and a novel platform for 3D stress-free manipulations.

DOI: [10.1103/PhysRevResearch.6.023234](https://doi.org/10.1103/PhysRevResearch.6.023234)

I. INTRODUCTION

Microfluidics enables the study of the behavior, control, and manipulation of microscale flows typically using device architectures comprising channels and junctions as their building blocks [1–4]. Desired flow structures and microfluidic functions such as transporting and mixing chemicals [5], shaping flow profiles [6,7], encapsulating multiphase fluids [8,9], and trapping microparticles [10,11] are incorporated through the geometry of these building blocks and the topology of their assemblies [12–15]. Despite this increased complexity, our understanding of these microfluidic functions is mostly achieved in a case-by-case fashion relying on actual experimental measurements or on computational fluid dynamics (CFD) studies using detailed experimental geometries. A unified framework that allows us to understand how these complex flow structures emerge from simpler, more fundamental flows would prove extremely useful for the fast, modular development of rationally designed flow structures and associated microfluidic functions.

Symmetry is a concept that has been used to understand phenomena and structures in disciplines ranging from fundamental physics to viral structure [16–18]. In the realm of microscale flows, symmetries are essential features of representative flow structures, such as the helical symmetry in swimming microorganisms [19,20] and the reflection symmetry applicable in many hydrodynamic interactions [21,22]. These symmetries have profound implications with

helical symmetry giving rise to swimming motility in bacterial species due to the breaking of kinematic reversibility while the reflection symmetries possessed by a pair of microswimmers constrain their synchronization and thus their collective motion. Such considerations applied to microfluidic systems could allow us to uncover very general results independent of system details. Recent work on multi-channel microfluidic junctions and open-space microfluidics have shown that their main flow structures can be obtained from the potential flows around charges representing the channels' ports, without consideration of detailed channel geometries [11,23]. This simplification has revealed intriguing flow structures that enable rich microfluidic applications, such as flow-driven traps for particle manipulation and dynamic confinements of fluid into multipolelike networks. Additionally, certain combinations of rotation and reflection symmetries have been applied both analytically and numerically to a multi-port microfluidic junction to eliminate strain components at the junction center, giving rise to potentially perturbation-free micromanipulations [24]. All the above implications of symmetries suggest the feasibility of using a more generalized symmetry-based approach, i.e., the symmetry group, for a more fundamental understanding of the origins of these symmetries and ways to manipulate them for specific functions.

One of the most desirable of these microfluidic functions is manipulating flow structures that allow the displacement of individual microscale objects along arbitrary paths [25]. Typically, micromanipulation techniques involve trapping particles using electromagnetic, acoustic, or flow fields that produce restoring forces in the vicinity of the trap [26–29]. For example, in cases where hydrodynamic flow alone is used for trapping, previous studies have shown that a Stokes trap can be achieved by managing the locations of hyperbolic points through multiple channels that intersect at a middle junction [11]. The location of such a trap can be dynamically adjusted to realize the direct manipulation of trapped particles, which has also been extended to 3D flows very recently [30].

*Corresponding author: bliu27@ucmerced.edu

Published by the American Physical Society under the terms of the Creative Commons Attribution 4.0 International license. Further distribution of this work must maintain attribution to the author(s) and the published article's title, journal citation, and DOI.

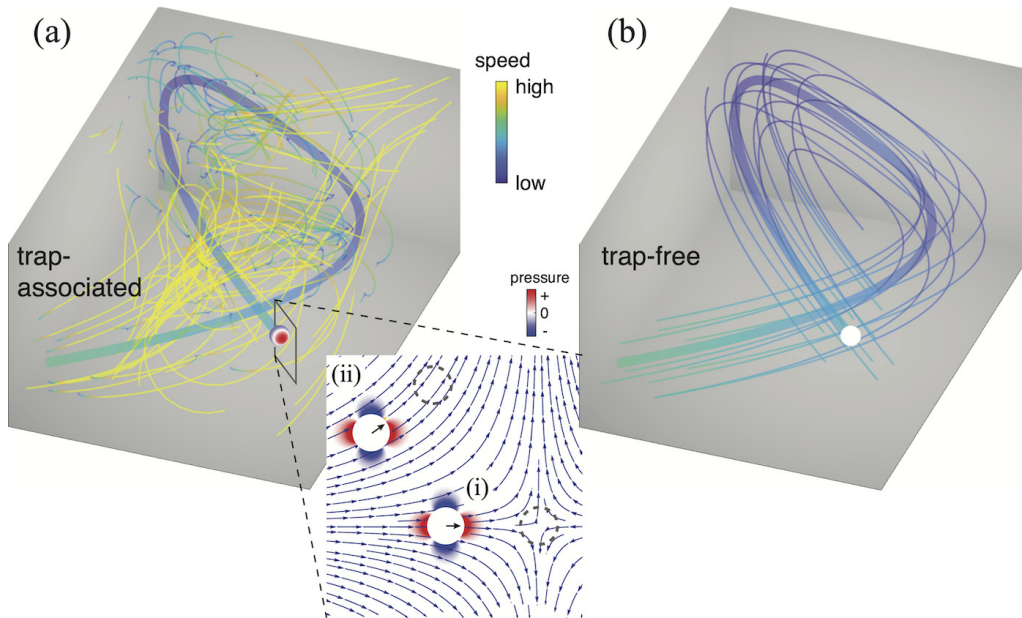


FIG. 1. Trap-associated vs trap-free manipulations of microscale particle through surrounding flows. (a) In trap-associated manipulations, a manipulated particle is led by a fluid “trap” or guided by the local flow director [zoomed-in 2D views (i) and (ii) in the inset, respectively] along the desired pathway (shown in the thick curve), surrounded by overall divergent flows (with speeds of fluid tracers shown in colors) due to its trapping nature. The stress distribution around the particle (with dashed circles showing target positions) is intrinsic to the far-field flow topology (inset), with compression (in red) and extension (in blue) along orthogonal axes, independent of its relative position to the trap. (b) An ideal perturbation-free manipulation is achieved by entraining the particle in a uniform flow field. All surrounding fluid flows in parallel paths at identical velocities and leaves the entrained particle stress-free (in blank color).

Computation-assisted feedback-control has also enabled manipulations of particles along local flow fields without the explicit employment of a hyperbolic point [25,31]. The displacements of particles can be adjusted by aligning the local flow field with the moving directions of particles. However, even without the presence of a local hyperbolic point, trapping and displacement are inextricably coupled. As illustrated in Fig. 1(a), flow fields far from these locally hyperbolic-point-free flows can be divergent, leading to inevitable stress perturbations on any manipulated objects. It is worth noting that the stress distribution on the particle is intrinsic to the far-field hyperbolic topology [32]. Even for a flow field that appears uniform, e.g., within a locally trap-free zone in Fig. 1(a) inset, the stress distribution on the entrained particle is identical to that within the trap, regardless of their relative displacement. These stressful perturbations thus restrict such approaches to studying stress-insensitive phenomena. Scaling such approaches with traps or local flow vector fields to simultaneously manipulate large numbers of particles is also a challenge. Here, we explore the use of symmetry groups to guide the design of microfluidics that enable multiplexed and stress-free manipulation, which is characterized by a truly uniform flow field around the manipulated particle(s) [Fig. 1(b)]. Distinct from the above locally uniform flows (as exemplified in Ref. [31]), the instantaneous flow field here is strictly parallel and straight, avoiding any hyperbolic point in the far field or even outside the microfluidic boundaries (as depicted through symmetries, shown below). Specifically, we identify and characterize microfluidic flow structures based on symmetry groups, which allow us to distinguish and robustly realize fundamentally different microfluidic functions.

II. SYMMETRIES IN MICROFLUIDIC SYSTEMS

A. 2D Microfluidic symmetries

We start with a cross-channel junction for its well-understood microfluidic functions and relatively simple symmetries. Here, the four ports of identical channels (with flow rates f_i , $i = 1, 2, 3, 4$) form a square [Fig. 2(a)], and therefore its flow structures in the plane are restricted by the symmetry of a square. An arbitrary flow pattern generated by a combination of $\{f_i\}$ at this junction corresponds to a set of identical flow manipulations through certain rotations or reflections (Appendix B). All such possible rotations or reflections (including the trivial identity operation) form a dihedral-4 (D4) symmetry group [16], which restricts the possible flow patterns. This D4 group thus represents the flow manipulation functions in a cross-channel junction. How do the D4 group elements map to the actual flow functions? Analogous to the subgroups contained in one symmetry group, these flow manipulation functions are reducible into smaller classes with unique features. We note first that there are only three independent flow modes, resulting from the number of controls (four channels) minus the number of constraints (one associated with the conservation of volume, i.e., $\sum_{i=1}^4 f_i = 0$). Through inspection, one can readily identify these three modes, forming two classes of flow functions. First, fluxes with opposite signs through a pair of opposing channels give rise to displacement flows along two orthogonal directions (x and y), corresponding to two fundamental modes [Fig. 2(b)]. Second, fluxes with same sign through both pairs of opposing channels provide one more fundamental elongation flow mode [Fig. 2(c)]. Any flow profile produced in this junction [with

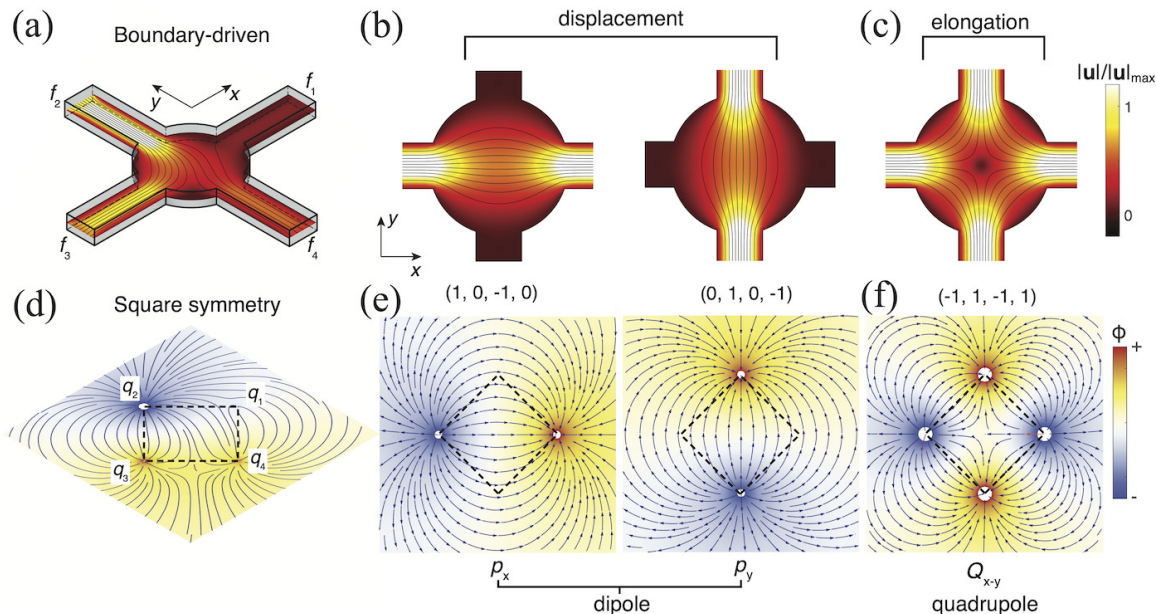


FIG. 2. Functional classification of a cross-channel microfluidic junction. (a) A 2D CFD simulation of the flow pattern (with streamlines in solid curves and speed $|\mathbf{u}|$ in colors) from an arbitrary flux setting ($f_1 - f_4$ at four ports) can be decomposed into three linearly independent flow modes: (b) two orthogonal displacement flow modes, and (c) one elongation flow mode. (d) The flow pattern in (a) is reproduced by a flow potential ϕ associated with fluid sources (or sinks) at the four corners of a square ($q_1 - q_4$). The square symmetry gives rise to (e) two degenerate dipole modes equivalent to two displacement modes in orthogonal directions, and (f) one quadrupole mode equivalent to elongation flow.

an example shown in Fig. 2(a)] must be a combination of these three flow modes. However, none of these fundamental modes can be generated by combining any of the rest, a consequence of their linear independence. Importantly, the two displacement modes have a reflection symmetry (along 45° from the x axis), forming a reflection group D1 or a cyclic group C2, which is known to be a subgroup of the D4 group [33]. The single elongation flow mode also represents a trivial subgroup of D4 that contains only the identity operation. In addition to forming different subgroups, these two classes of flows also have distinct characteristic functions, here displacement versus elongation. To abstract these functions from the detailed flow geometries, we map the cross-channel junction to a square, where the flux at each channel is mapped to an effective charge at each lattice site (q_1, q_2, q_3, q_4), representing a pointlike fluid source (positive) or sink (negative). The flow field is thus well-defined as a potential flow, with the flow velocity \mathbf{u} given by the gradient of the potential ϕ , i.e., $\mathbf{u} = \nabla\phi$. Since the classes of flow functions are independent of the choice of coordinates, the candidate quantities for such purposes are the strain rate invariants [34] that do not change under any rotation of the microfluidic device. The first-order invariant I_1 , which is the trace of the rate of strain tensor $\dot{\gamma}$, is trivial and vanishes for incompressible fluids. We therefore consider the first nontrivial invariant $I_2 = -\frac{1}{2}\text{Tr}(\dot{\gamma}^2)$. For a 2D potential flow with a total number of $N = 4$ sources and sinks (with magnitudes $\{q_i\}$, located at $\{\mathbf{r}_i\}$), the scalar potential can be expressed as $\phi(\mathbf{r}) = \sum_{i=1}^4 q_i \ln(|\mathbf{r} - \mathbf{r}_i|)$. Since the rate of strain is linearly related to the magnitudes of sources (or sinks), we can show (Appendix C) that the invariant I_2 at the center of the junction has a quadratic form with respect

to q_i , i.e., $I_2 = \sum_{i,j=1}^4 L_{ij}q_iq_j$, where L_{ij} is the element of a coupling tensor, depending on the distance between the pair of q_i and q_j . On a square, there are only two possible types of pairs: pairs along the lateral sides or along the diagonals. With these considerations, we can show (Appendix C) that the \mathbf{L} tensor has the form

$$\mathbf{L} = \begin{bmatrix} 0 & a & b & a \\ a & 0 & a & b \\ b & a & 0 & a \\ a & b & a & 0 \end{bmatrix}. \quad (1)$$

Elements “a” and “b” are symbolic representations of the above lateral and diagonal couplings, respectively, forming a symmetric circulant matrix for \mathbf{L} . A circulant matrix has all the same rows with each row being rotated one element to the right relative to the row above. One mutual eigenvector for any circulant matrix corresponds to the trivial mode where all four charges are identical, i.e., $(q_1, q_2, q_3, q_4) = (1, 1, 1, 1)$. This mode cannot be accessed by a fluid system due to the invalidation of the continuity condition. This leaves $N - 1 = 3$ nontrivial eigenmodes (all satisfying $\sum_{i=1}^4 q_i = 0$), in agreement with the degrees-of-freedom argument. Every nontrivial mode exhibits a one-to-one map to the fluidic manipulation function as previously classified through subgroups of the D4 group [Fig. 2(d)]. It is worth noting that a hyperbolic point outside the original fluid boundary [indicated by dashed lines in Fig. 2(d)] becomes visible through this symmetry representation of the flow, identifying any potential “trapping” component of a flow pattern. More specifically, the degeneracy of two orthogonal dipoles corresponds to a common displacement function of the flow along orthogonal directions

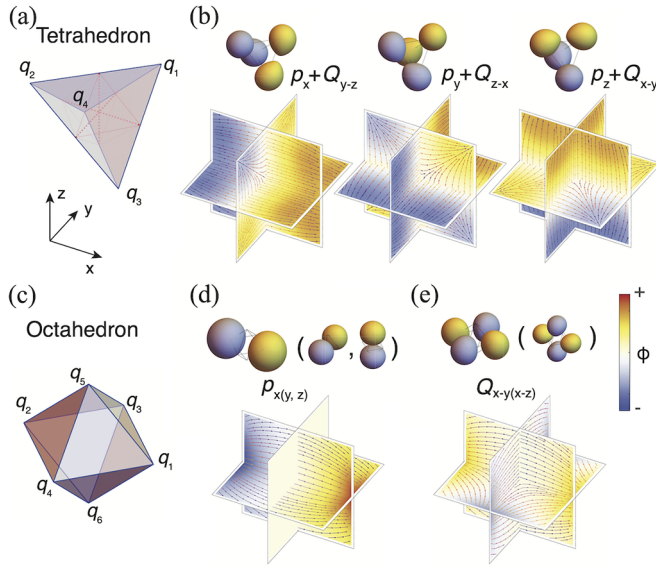


FIG. 3. Microfluidic devices with 3D symmetries. (a) Fluid sources (or sinks) following a tetrahedral symmetry ($q_1 - q_4$) can be classified into three degenerate functions, (b) a mix of dipole p and quadrupole Q in each of the three orthogonal directions, representing simultaneous displacement and elongation of the fluid. (c) Fluid sources (or sinks) following an octahedral symmetry ($q_1 - q_6$) can be classified into two subgroups: (d) three dipoles along orthogonal directions (x , y and z) and (e) two quadrupoles in orthogonal planes (e.g., x - y and x - z), contributing to separate displacement and elongation functions.

[Fig. 2(e)]. The remaining quadrupole-like mode is nondegenerate and maps to the elongation function [Fig. 2(f)].

B. 3D Microfluidic symmetries

As demonstrated above, the eigenvalue analysis of the stress invariant (I_2) provides an automatic strategy of classifying microfluidic functions, which we now extend to 3D structures to incorporate more sophisticated symmetries. The potential flow now adopts its 3D form with N sources, $\phi(\mathbf{r}) = \sum_{i=1}^N -\frac{q_i}{|\mathbf{r}-\mathbf{r}_i|}$. For relatively more practical applications in microfluidics, we consider here the 3D symmetries contained in structures with fewer vertices, namely the tetrahedron ($N = 4$) and the octahedron ($N = 6$).

A tetrahedron has a permutation S_4 symmetry [33], corresponding to an unaltered structure (identical through rotation and reflection) by permuting all four vertices [Fig. 3(a)]. The eigenvalue analysis shows that all three eigenmodes for this tetrahedron are degenerate [Fig. 3(b)], due to equivalent neighbors for every vertex. These three modes together represent a threefold rotation symmetry group (C_3) (achieved by 120° rotation about any of the face norms), which is a subgroup of S_4 . Notably, the potential flow of such a mode exhibits a mixture of dipole and quadrupole moments [upper Fig. 3(b)], leading to a microfluidic function corresponding to simultaneously displacing and elongating (transverse to the displacement axis) the fluid within the junction. To obtain a purely displacing flow in 3D, we therefore look to the next available polyhedral symmetry, i.e., the octahedral symmetry.

An octahedron [Fig. 3(c)] can be formed by the middle points of the six edges of a tetrahedron [Fig. 3(a)]. Its symmetry group is isomorphic to $S_4 \times C_2$, with the additional symmetry arising from an extra twofold rotation symmetry that is absent for a tetrahedron [Fig. 3(a)] [33]. A similar eigenvalue analysis leads to two groups of degenerate modes, corresponding respectively to dipoles and quadrupoles. The three degenerate dipole modes (p_x , p_y , p_z) are orthogonal in direction, corresponding to a C_3 group (through 120° rotation about any of the face norms), one subgroup of the octahedral symmetry group [33]. In such dipole modes, a pair of effective charges along the diagonal (e.g., q_1 and q_2 for p_x) have opposite signs (with the rest of the charges being neutral), corresponding to the activation of a pair of a source and a sink. The two degenerate quadrupoles are distributed in two perpendicular planes (here, x - y and x - z planes), forming a D_1 subgroup (switchable by a reflection along the middle plane between x - y and x - z planes). In such quadrupole modes, a pair of sources and a pair of sinks along two diagonals are activated. It should be noted that an equivalent quadrupole in the y - z plane can be achieved by superimposing the above two quadrupoles, and is thus not one of the eigenmodes. Analogous to the square symmetry in the 2D case, the octahedral symmetry gives rise to completely separate displacement and elongation flow functions [Figs. 3(d) and 3(e)], classified by distinct symmetries. The pure-dipole-like potential in the displacements also ensures that the rate-of-strain invariant I_2 is zero in the middle of the junction. Thus, a superposition of these three displacement flow modes generates 3D omnidirectional flows while preserving the stress-free condition (at least in the middle of the junction).

III. REALIZING 3D STRESS-FREE MICROFLUIDIC MANIPULATIONS

A. Omnidirectional stress-free flows

To realize such a stress-free microfluidic junction while enabling microscope observation, we rotate the octahedron so that one of its faces [e.g., (1,1,1) axis] is aligned along the visualization axis (z'). This rotated geometry fits well into a double-layer microfluidic design [24]: six channels (0.5 mm wide and 0.3 mm deep in cross-sections) at two elevations intersecting a middle cylindrical chamber (with radius $R = 1.0$ mm and height $H = 1.6$ mm) along the radial directions, with the locations of intersections matching that of the octahedral vertices [Fig. 4(a)]. This rotation is also determined by the coordinates of the laboratory frame of reference (x' , y' , z'), with a radial channel (here, f_1) aligned along the x' axis. We fabricated the microfluidic channel part of this device by fusing multiple sheets of laser-etched glass (Citrogene, Inc., see Appendix A), which was then mounted on a customized adapter for flow control and microscopy.

To ensure that a displacement flow can be robustly created in all possible directions, we first considered flows along the three orthogonal axes (x' , y' , z') of the laboratory coordinates forming the basis of the velocity space. The potential representations (isosurfaces) of these orthogonal flows (along x' , y' , and z') are shown in Fig. 4(b), which are linear combinations of the above three degenerate dipole modes with their

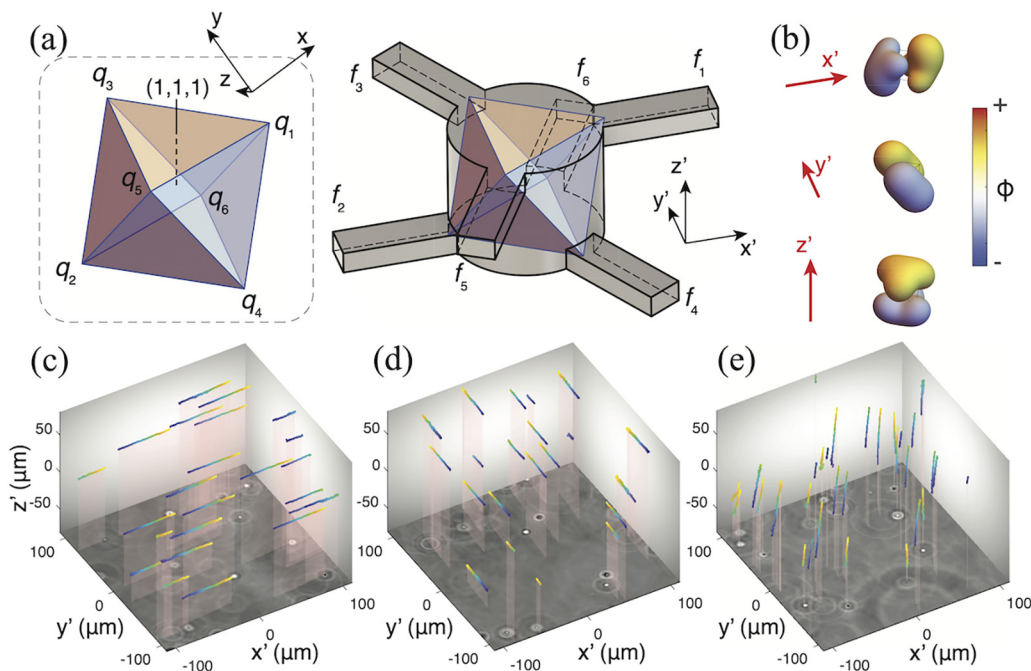


FIG. 4. Realization of the octahedral symmetry in 3D microfluidics. (a) An octahedron viewed along its original (1,1,1) axis (inset) is converted into a microfluidic junction with all sources (or sinks) distributed at two planes perpendicular to the imaging axis z' . (b) The dipole flows in microscope coordinates (x', y', z') are obtained by linear combination of the three orthogonal dipole modes [Fig. 3(d)], with their experimental realizations shown in (c), (d), and (e), respectively. The axial z' positions of the seeding particles are obtained by correlating their phase-contrast images (projected in the bottoms of volumes) with a calibrated library of diffraction patterns.

coefficients (c_1, c_2, c_3) being $\frac{1}{\sqrt{6}}(2, -1, -1)$, $\frac{1}{\sqrt{2}}(0, 1, -1)$, and $\frac{1}{\sqrt{3}}(1, 1, 1)$, respectively. In experiments, these effective charges are realized by independently offsetting the fluid pressure on the corresponding channel using two 4-channel piezoelectric regulators (Elveflow OB1 MK3+), with a positive offset for a positive charge (or source) and a negative offset for a negative one (or sink). Custom software was programed to convert the above flow coefficients into actual pressure settings for flow generation (Appendix A). The three orthogonal flows (x', y', z') were successfully generated in our microfluidic device, within the same volume near the center [Figs. 4(c)–4(e)], as demonstrated by the 3D traces of the seeding particles (Appendix A). Despite their different geometries in flow dipoles [Fig. 4(b)], these flows are all uniform over almost the entire 3D volume ($\approx 200 \mu\text{m} \times 200 \mu\text{m} \times 150 \mu\text{m}$) captured by the microscope, demonstrating the experimental realization of a robust “stressless” condition that is guaranteed by symmetry.

B. Dynamic stress-free micromanipulations

To further investigate the experimental capacity of such stress-free microfluidics, we incorporated temporal dependence in the flow by dynamically varying the pressures on all channels. To facilitate this time-dependent control, we represented each possible configuration of the displacement flow by its coefficients (c_1, c_2, c_3) when expressed in terms of three degenerate dipole modes, which essentially form a 3D phase space [Fig. 5(a)]. Any time-dependent flow manipulation can thus be generated by a series of points in this

phase space (Appendix D). Noting that an axial (z') flow is represented by a vector along the $\frac{1}{\sqrt{3}}(1, 1, 1)$ direction in the phase space, all orthogonal flows must satisfy $c_1 + c_2 + c_3 = 0$, which restricts all horizontal (or in-plane) displacement flows to a plane in the phase space. Hopping in this plane with equal angular separations and distances with respect to the origin (0,0,0) gives rise to polygon-shaped flow patterns, for instance, a triangle, a square and a circle in the continuum limit [Figs. 5(b)–5(d), movies S1–S3 [35]]. Such patterns are almost identical for all seeding particles, with the fluid in the bulk translating like a piece of solid.

By incorporating phase spaces out of the $c_1 + c_2 + c_3 = 0$ plane, we also generated time-dependent flows in 3D. For instance, imposing an oscillatory z' motion (with doubled frequency) to the above circular mode gives rise to a 3D flow that represents a Lissajous curve [Fig. 6(a), movie S4 [35]]. Invariably, individual seeding particles within the volume of observation trace out the same pattern as desired, demonstrating the robustness of the stressless condition even under 3D dynamic control.

To assess the flow uniformity, we center the trajectory of every seeding particle within the entire volume and show them side by side. It is clear that these trajectories overlap with each other very well over a full period. In perfectly stress-free flows, all trajectories must be identical, leaving no deviation from the mean path. We thus defined a characteristic strain based on the deviation from the mean trajectory, i.e., $\epsilon(t) = \text{deformation/size} = \frac{\Delta \tilde{r}(t)}{\Delta r(t)}$, where $\Delta r \equiv \sqrt{\langle (\mathbf{r} - \langle \mathbf{r} \rangle) \cdot (\mathbf{r} - \langle \mathbf{r} \rangle) \rangle}$ and $\Delta \tilde{r}(t) \equiv \sqrt{\langle (\tilde{\mathbf{r}} - \langle \tilde{\mathbf{r}} \rangle) \cdot (\tilde{\mathbf{r}} - \langle \tilde{\mathbf{r}} \rangle) \rangle}$ are the fluctuations of

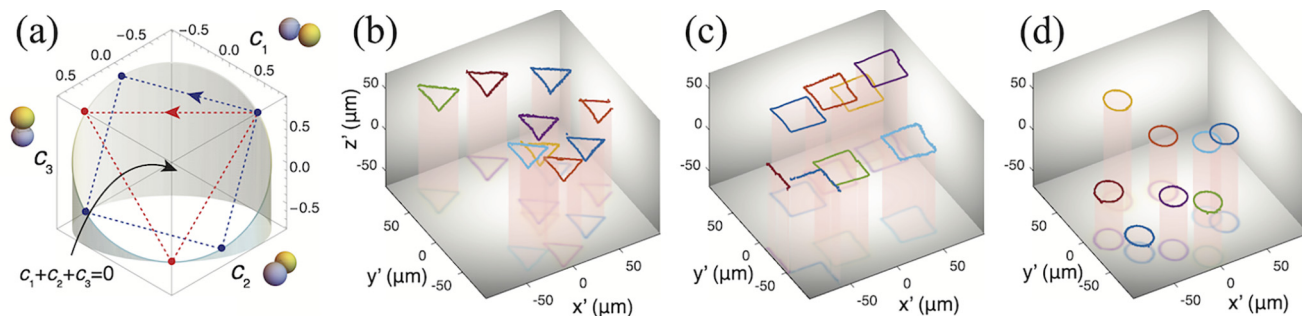


FIG. 5. Dynamic stress-free displacement flows in 2D. (a) Stress-free displacement flows were controlled in a phase space (c_1, c_2, c_3), as the components of three orthogonal dipole modes. Traces in the $c_1 + c_2 + c_3 = 0$ plane of this phase space correspond to in-plane flows (in the $x'-y'$ plane) in the real space. The dashed lines correspond to instantaneous transitions between discrete states (dots) of the flow with the arrow showing the transition directions, forming a triangle, a square, and a circle in the continuous limit. The corresponding motions of the flow are shown in (b), (c), and (d), respectively, with individual seeding particles shown in different colors. The periods of these patterns are 3 s, 4 s, and 4 s, respectively.

displacements of all particles (\mathbf{r}) before [Fig. 6(a)] and that ($\bar{\mathbf{r}}$) after [Fig. 6(b)] centering, with operators $\langle \cdot \rangle$ corresponding to spatial averages. As shown in Fig. 6(c), such characteristic strains are of the order of $\epsilon \sim 10^{-2}$ for typical 3D manipulations, illustrating the nearly stress-free condition.

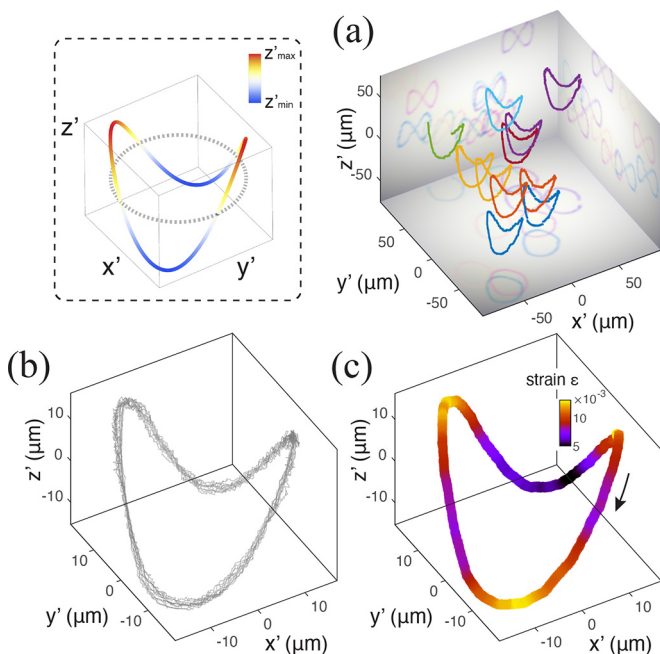


FIG. 6. 3D stress-free and multiplexed manipulation. (a) A design of the 3D Lissajous pattern (inset, with 3D positions in color and 2D projections in gray) was realized in the flow by incorporating additional axial motion into the circular pattern [Fig. 5(d)], with all seeding particles in the view tracing out the desired 3D pattern (in 8 s). (b) Visualized trajectories (gray curves) of seeding particles (11 particles shown) within the 3D view ($200 \mu\text{m} \times 200 \mu\text{m} \times 150 \mu\text{m}$ in $x' \times y' \times z'$) were overlaid and exhibited a fair degree of uniformity. (c) A characteristic strain ϵ computed along the manipulation path further confirms the uniformity (with ϵ bounded by 2%) of the manipulation flows.

The agile flow responses to the controlling pattern in the phase space indicate a direct map of the phase space to the real velocity space. The previously mentioned control in phase space can thus be generalized to arbitrary flow motions to realize more sophisticated manipulation capabilities. To demonstrate this concept, we combine both continuous motions and discrete hops in the phase space (or the velocities) to manipulate, in a stress-free manner, individual particles for “printing” discrete letters (here, “UCM”) onto the focal plane. Each letter was traced out by combining motions (along smooth curves) and hops (at the corners of the letter) in the phase space. The discrete gaps between adjacent letters were achieved by abruptly offsetting the fluid in the axial direction so that the previously focused particles were moved away from the focal plane before their reappearance for “printing” the next letter. As shown in Fig. 7, this “printing” task can indeed be achieved in our stress-free microfluidic channel, which further demonstrates its versatile manipulation capabilities (movie S5 [35]).

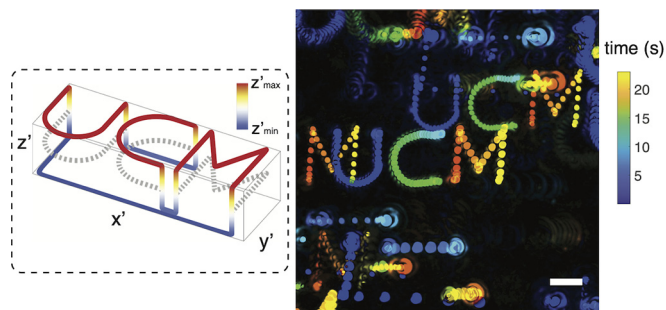


FIG. 7. More complex 3D flow manipulations were demonstrated by rapidly imprinting the “UCM” (with its design shown in the inset) onto the focal plane by seeding particles, which are color-coded in time (over 23 s). Some of those particles initially out of the focal plane imprint the connecting lines (blue segments in the inset) between letters. The scale bar shows $20 \mu\text{m}$.

IV. DISCUSSION

Our results show a substantial role for symmetry groups in classifying microfluidic functions. These symmetry-group-protected functions are insensitive to detailed geometries, which we exploited to realize 3D stress-free flows in a microfluidic device. Such flows are qualitatively different from all available micromanipulation approaches, where physical traps of certain forms must be present, resulting in stresses on the manipulated objects. Both the stress-free modes and the stressful modes can be characterized by distinct subgroups of a group of polyhedral symmetry (possessed by the microfluidic device), suggesting independent transport and trapping in microfluidic manipulations.

From our experimental observations, these stress-free flows are demonstrated by extremely parallel trajectories of the manipulated particles, regardless of the detailed curvatures of the trajectories. This enables us to achieve truly multiplexed stress-free manipulations, a significant challenge for trap-based approaches. It is worth noting that our trajectories inevitably deviate from the ideal geometries due to the absence of feedback controls. Meanwhile, any potential differences (e.g., different flow resistances) among the six channels lead to channel-sensitive responses to applied pressures, which ultimately modifies our time-dependent flow patterns. Remarkably, these “defects” in manipulations do not alter the uniformity in the flows (with all particle trajectories remaining parallel), suggesting the robustness in the symmetry-protected flows.

Our work therefore opens up new avenues of experiments on microscopic phenomena that occur in truly stress-free flows. Combinations of the above subgroups easily lead to other subgroups with higher orders (e.g., the C4 subgroup of the D4 group), associated with flow characteristics more than the strain invariants at the center. Flow patterns belonging to these subgroups maybe coordinated in time to form a mutual impact on the manipulated flow, e.g., creating a “mean” vortex that is absent from steady potential flows. These advanced symmetry features and flow manipulation functions will be explored in our future work.

ACKNOWLEDGMENTS

This work was supported by National Science Foundation Grants No. CBET-2046822 and No. CBET-1706511, NSF-CREST: Center for Cellular and Bio-molecular Machines (CCBM) at UC Merced (HRD-1547848), and Department of Defense DURIP ARO No. 73839-MA-RIP. A.G. also acknowledges partial support from the NSF Center for Engineering Mechanobiology Grant No. CMMI-154857.

APPENDIX A: EXPERIMENTAL METHODS

1. Microfluidic fabrication and its assembly for microscope observations

The microfluidic channel was fabricated as a stack of glass sheets (0.13–1 mm thick), with each containing a special pattern of channels. We made the design of these sheets through a computer assisted design (CAD) software (Autodesk Fusion 360), which were then sent to Citrogene for fabrications of these customized sheets in borosilicate glass and their

integration into one single multilayer microfluidic chip (using optically clear adhesives). The overall exterior dimension of the microfluidic chip is compact, here, 62 mm × 22 mm × 2.7 mm in x , y , and z , comparable to the footprint of a typical glass slide. The chip was also designed to be self-enclosed, leaving only 6 small pores (1 mm in diameter) open for accessing the microfluidic flows. A 0.13 mm thick glass sheet at the bottom layer sealed the microfluidic channels and enabled high optical quality for conventional microscope observations. Before being connected to a multichannel pump, the glass chip was mounted to a customized adapter for better sealing results.

2. Multiple-channel flow controls

Flows within the multilayer microfluidic channel were generated by two four-channel microfluidic flow controllers (Elveflow OB1 MK3+) with each channel’s pressure regulated independently between -0.9 and 1 bar relative to the atmospheric pressure. A custom program (written in PYTHON) was used to modulate the pressures on each channel and record the microscope image in real time. To accommodate the finite resolution of our pressure controllers, here 120 μ bar, we used a water-glycerol mixture to increase the viscosity of the fluid in the microfluidic channel, which maintained the flow speed within a reasonable range for microscope observations while using a decent fraction of the pressure range.

3. Microscope imaging and three-dimensional flow reconstructions

The microfluidic flows were visualized by mixing the fluid with polystyrene beads (2 μ m in diameter) as seeding particles, imaged under an inverted microscope (Nikon Eclipse Ti2) at a 60 \times magnification, operated in its phase-contrast mode. These phase-contrast images were recorded by a USB Scientific CMOS (sCMOS) video camera (Andor Zyla 4.2) in full resolution (2048 × 2048 pixels) at 50 fps. The diffraction pattern of each seeding particle was visible within a range of 160 μ m along the optical axis, which were calibrated to restore the axial positions of all seeding particles in the view [36], forming a sizable (at least 200 μ m × 200 μ m × 100 μ m) visible zone of the 3D flow field.

APPENDIX B: MICROFLUIDIC REPRESENTATIONS OF SYMMETRY GROUPS

The possible ways of generating essentially equivalent flow patterns (regarding their functions) define the symmetry of a microfluidic device. For instance, a random flow (with the same pattern) can be generated in a total of eight different ways in a four-channel cross junction (Fig. 8). These eight ways compose the symmetry group of a dihedral-4 (D4) symmetry [37]. A subset within this group can also be arranged to form a smaller group of symmetry, a subgroup of the D4 group. For instance, either the upper or the lower row forms a cyclic-4 (C4) symmetry, with each element accessible through a fourfold rotation. A pair of adjacent elements along the vertical or the horizontal direction forms a D1 subgroup (for the reflection symmetry along the horizontal axis). A pair of

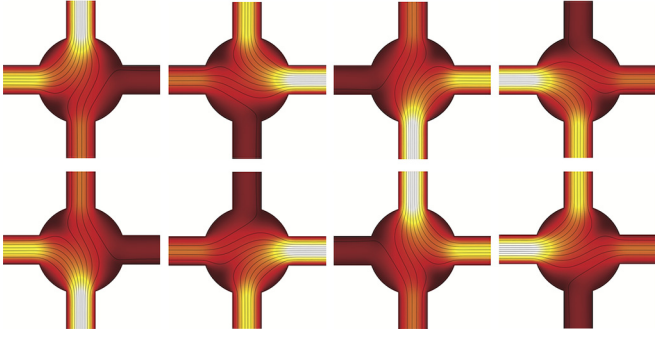


FIG. 8. Symmetry in a four-channel microfluidic junction. A total of eight equivalent flow patterns (regardless of rotation and reflection) are accessible in the same microfluidic junction, representing a D_4 symmetry.

the adjacent elements along the diagonals also forms a D_1 subgroup, however, for a reflection along a certain 45° axis.

APPENDIX C: SYMMETRIES IN THE STRAIN-RATE INVARIANT

We consider a junction in a microfluidic device actuated by a set of infinitesimal sources or sinks and ignore the detailed boundary condition. The flow can thus be characterized by a potential flow set by fluid sources [38]. For a 2D junction, the flow velocity \mathbf{u} can be determined from a potential ϕ as [11,23]

$$\mathbf{u}(\mathbf{r}) = \nabla\phi(\mathbf{r}), \quad (\text{C1})$$

$$\phi(\mathbf{r}) = \sum_{i=1}^N q_i \ln(|\mathbf{r} - \mathbf{r}_i|), \quad (\text{C2})$$

$$\dot{\gamma}^2 = \sum_{i,j} \frac{q_i q_j}{|\mathbf{r} - \mathbf{r}_i|^2 |\mathbf{r} - \mathbf{r}_j|^2} \left[\mathbf{I} - 2 \frac{(\mathbf{r} - \mathbf{r}_i)(\mathbf{r} - \mathbf{r}_i)}{|\mathbf{r} - \mathbf{r}_i|^2} - 2 \frac{(\mathbf{r} - \mathbf{r}_j)(\mathbf{r} - \mathbf{r}_j)}{|\mathbf{r} - \mathbf{r}_j|^2} + 4 \frac{(\mathbf{r} - \mathbf{r}_i)(\mathbf{r} - \mathbf{r}_i) \cdot (\mathbf{r} - \mathbf{r}_j)(\mathbf{r} - \mathbf{r}_j)}{|\mathbf{r} - \mathbf{r}_i|^2 |\mathbf{r} - \mathbf{r}_j|^2} \right]. \quad (\text{C8})$$

Then, taking the trace we conclude

$$I_2 = -\frac{1}{2} \text{tr}(\dot{\gamma}^2) = \sum_{i,j} -\frac{q_i q_j}{2|\mathbf{r} - \mathbf{r}_i|^2 |\mathbf{r} - \mathbf{r}_j|^2} \left[-1 + 4 \frac{[(\mathbf{r} - \mathbf{r}_i) \cdot (\mathbf{r} - \mathbf{r}_j)]^2}{|\mathbf{r} - \mathbf{r}_i|^2 |\mathbf{r} - \mathbf{r}_j|^2} \right]. \quad (\text{C9})$$

Finding those independent flow modes (functions) thus becomes an eigenvalue problem. The symmetries of a microfluidic junction are embedded in the $\mathbf{L}(\mathbf{r})$ matrix. We consider here the invariant at the center of the junction, $I_2(\mathbf{0})$, where most symmetries in a device must apply.

For fluid sources lying on the four corners of a square, the matrix $\mathbf{L}(\mathbf{0})$ complies with the symmetries of a square, i.e., the D_4 group. The $\mathbf{L}(\mathbf{0})$ matrix that satisfies this symmetry group can be represented by

$$\mathbf{L}(\mathbf{0}) = \begin{bmatrix} 0 & a & b & a \\ a & 0 & a & b \\ b & a & 0 & a \\ a & b & a & 0 \end{bmatrix}. \quad (\text{C10})$$

where q_i and $\mathbf{r}_i = (x_i, y_i)$ are the magnitude and location of each source, respectively. Consequently,

$$\mathbf{u}(\mathbf{r}) = \sum_{i=1}^N q_i \frac{\mathbf{r} - \mathbf{r}_i}{|\mathbf{r} - \mathbf{r}_i|^2}. \quad (\text{C3})$$

The rate of strain tensor of the flow is thus

$$\dot{\gamma} = \frac{1}{2} [\nabla\mathbf{u} + (\nabla\mathbf{u})^\top], \quad (\text{C4})$$

$$\dot{\gamma} = \sum_{i=1}^N \frac{q_i}{|\mathbf{r} - \mathbf{r}_i|^2} \left[\mathbf{I} - 2 \frac{(\mathbf{r} - \mathbf{r}_i)(\mathbf{r} - \mathbf{r}_i)}{|\mathbf{r} - \mathbf{r}_i|^2} \right]. \quad (\text{C5})$$

Since a function of a microfluidic device should be independent of the choice of coordinates, we consider the invariant of the rate of strain tensor [34]. The first nontrivial invariant is its second-order invariant

$$I_2 = -\frac{1}{2} \text{Tr}(\dot{\gamma}^2). \quad (\text{C6})$$

From the scaling, it can be shown that the invariant I_2 has a quadratic form of q_i , i.e.,

$$I_2(\mathbf{r}) = \mathbf{q}^\top \cdot \mathbf{L}(\mathbf{r}) \cdot \mathbf{q} = \sum_{i,j=1}^N L_{ij}(\mathbf{r} - \mathbf{r}_i, \mathbf{r} - \mathbf{r}_j) q_i q_j, \quad (\text{C7})$$

where L_{ij} is a function of $\mathbf{r} - \mathbf{r}_i$ and $\mathbf{r} - \mathbf{r}_j$, which can be obtained explicitly by the above expressions.

Explicit construction of the second-order invariant is straightforward. Squaring Eq. (C5), we find

Such a matrix belongs to the category of circulant matrices [39], and the eigenvectors are expressed in the following:

$$v_1 = \frac{1}{\sqrt{2}}(1, 0, -1, 0),$$

$$v_2 = \frac{1}{\sqrt{2}}(0, 1, 0, -1),$$

$$v_3 = \frac{1}{2}(1, -1, 1, -1),$$

$$v_4 = \frac{1}{2}(1, 1, 1, 1).$$

Here, the first two modes are degenerate, corresponding to two dipole moments in orthogonal directions. The third mode

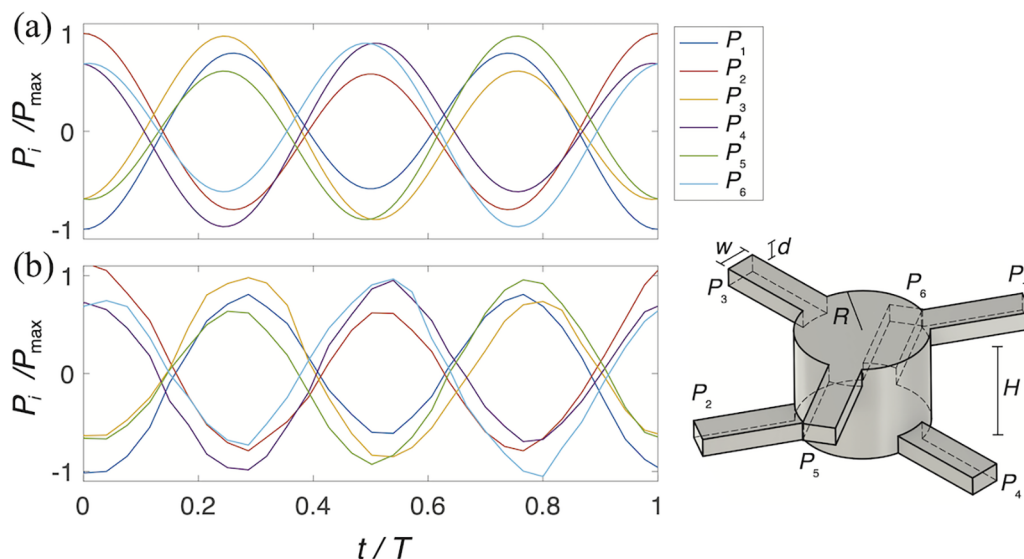


FIG. 9. Pressure regulations for stress-free microfluidic flows. (a) Six smooth time-dependent pressure curves $P_1 - P_6$, normalized by the maximal pressure $P_{\max} = 11$ mbar, were designed (as functions of time t) and applied to a six-channel microfluidic device (inset). Here, the curves correspond to the ideal ones for generating a 3D Lissajous flow (with a period $T = 8$ s). (b) The actual pressures monitored (by the pressure regulator) during the experiment show a consistent pattern.

corresponds to a quadrupole. The fourth mode is trivial and is excluded due to its contradiction with the continuity condition (for incompressible flows). It is worth noting that the diagonal zeros in $\mathbf{L}(\mathbf{0})$ can be replaced by any values, which only offset all eigenvalues by a constant.

The matrix $\mathbf{L}(\mathbf{0})$ can be explicitly found. We take as a choice of fluid locations a radial displacement $l/\sqrt{2}$ (for a square with lateral length l)

$$\mathbf{r}_1 = l/\sqrt{2}\hat{x}, \quad (\text{C11})$$

$$\mathbf{r}_2 = l/\sqrt{2}\hat{y}, \quad (\text{C12})$$

$$\mathbf{r}_3 = -l/\sqrt{2}\hat{x}, \quad (\text{C13})$$

$$\mathbf{r}_4 = -l/\sqrt{2}\hat{y}. \quad (\text{C14})$$

From Eq. (C9), these locations yield

$$\mathbf{L}(\mathbf{0}) = -\frac{2}{l^4} \begin{bmatrix} 3 & -1 & 3 & -1 \\ -1 & 3 & -1 & 3 \\ 3 & -1 & 3 & -1 \\ -1 & 3 & -1 & 3 \end{bmatrix} \quad (\text{C15})$$

$$= -\frac{2}{l^4} \left(3\mathbf{I} + \begin{bmatrix} 0 & -1 & 3 & -1 \\ -1 & 0 & -1 & 3 \\ 3 & -1 & 0 & -1 \\ -1 & 3 & -1 & 0 \end{bmatrix} \right), \quad (\text{C16})$$

thus matching the anticipated form of Eq. (C10) with an additional constant multiple of the identity matrix.

APPENDIX D: DYNAMIC STRESS-FREE FLOW GENERATIONS

To realize a dynamic stress-free flow pattern, we superimpose the three orthogonal dipole-flow modes along the principal axes of an octahedron [x , y , and z in Fig. 4(a)], with their coefficients (c_1, c_2, c_3) determined in the 3D phase space. On octahedral vertices, the charge assignments for these three orthogonal dipoles are respectively $(-1, 1, 0, 0, 0, 0)$, $(0, 0, -1, 1, 0, 0)$, and $(0, 0, 0, 0, -1, 1)$, corresponding to the pressure setting on six microfluidic ports. Since the axes of the microscope observation [x' , y' , and z' in Fig. 4(a)] are along the unit vectors $\frac{1}{\sqrt{6}}(2, -1, -1)$, $\frac{1}{\sqrt{2}}(0, 1, -1)$, and $\frac{1}{\sqrt{3}}(1, 1, 1)$ respectively in the phase space, the corresponding pressure settings ($\mathbf{P}_{x'}$, $\mathbf{P}_{y'}$, $\mathbf{P}_{z'}$) for three orthogonal flow modes along these directions are given by

$$\begin{aligned} \begin{pmatrix} \mathbf{P}_{x'} \\ \mathbf{P}_{y'} \\ \mathbf{P}_{z'} \end{pmatrix} &= \begin{pmatrix} \frac{1}{\sqrt{6}} & 0 & 0 \\ 0 & \frac{1}{\sqrt{2}} & 0 \\ 0 & 0 & \frac{1}{\sqrt{3}} \end{pmatrix} \cdot \begin{pmatrix} 2 & -1 & -1 \\ 0 & 1 & -1 \\ 1 & 1 & 1 \end{pmatrix} \cdot \begin{pmatrix} -1 & 1 & 0 & 0 & 0 & 0 \\ 0 & 0 & -1 & 1 & 0 & 0 \\ 0 & 0 & 0 & 0 & -1 & 1 \end{pmatrix} \\ &= \begin{pmatrix} \frac{1}{\sqrt{6}} & 0 & 0 \\ 0 & \frac{1}{\sqrt{2}} & 0 \\ 0 & 0 & \frac{1}{\sqrt{3}} \end{pmatrix} \cdot \begin{pmatrix} -2 & 2 & 1 & -1 & 1 & -1 \\ 0 & 0 & -1 & 1 & 1 & -1 \\ -1 & 1 & -1 & 1 & -1 & 1 \end{pmatrix}. \end{aligned} \quad (\text{D1})$$

For a stress-free flow at given velocity $\mathbf{v}(t) = (v_{x'}, v_{y'}, v_{z'})$, the pressures on six ports $\mathbf{P}(t) = (P_1(t), P_2(t), \dots, P_6(t))$ can be expressed as

$$\mathbf{P}(t) = \mathbf{v}(t)^\top \cdot \begin{pmatrix} \sigma_{x'} & 0 & 0 \\ 0 & \sigma_{y'} & 0 \\ 0 & 0 & \sigma_{z'} \end{pmatrix} \cdot \begin{pmatrix} \mathbf{P}_{x'} \\ \mathbf{P}_{y'} \\ \mathbf{P}_{z'} \end{pmatrix}, \quad (\text{D2})$$

where the middle diagonal matrix is the resistance matrix of the channel at the center region. It can be easily shown that these diagonal elements ($\sigma_{x'}$, $\sigma_{y'}$, $\sigma_{z'}$) are identical for perfect octahedral symmetries. *In situ*, these elements are expected to be subjected to boundary geometries and detailed fluid properties, which can be calibrated experimentally. In our microfluidic system, these geometries (illustrated in the inset of Fig. 9) are given by the radius ($R = 1$ mm) and height ($H = 1.6$ mm) of the middle cylindrical chamber and the cross section ($w \times d = 0.5 \times 0.3$ mm²) of the channels. For the glycerol solution (99.6%) used in this experiment, the corresponding resistance matrix elements are $\sigma_{x'} \approx 0.22$ mbar s/ μm , $\sigma_{y'} \approx 0.19$ mbar s/ μm , and

$\sigma_{z'} \approx 0.68$ mbar s/ μm . We attribute this significantly higher resistance along the axial (z') direction to the higher constraints that were applied to the axial flows by the noslip top and bottom surfaces of the cylindrical chamber.

To demonstrate the capability of such stress-free flows for dynamic manipulations, we use the above algorithm to determine the pressure setting $\mathbf{P}(t)$ for a time-dependent 3D flow velocity $\mathbf{v}(t)$. Using the 3D Lissajous flow as an example, its velocity can be prescribed by $\mathbf{v}(t) = (a \cos(\omega t), a \sin(\omega t), b \cos(2\omega t))$. Given the ratio b/a and the angular frequency ω (here, $b/a = 1.78$ and $\omega = 0.79$ rad/s), the pressures on every port are readily computed by the above equation [Eq. (D1)], which are shown in Fig. 9(a). These computed pressure curves are fed into a USB-based multi-channel pressure regulator in real time (controlled by a computer) through custom software. The actual pressures applied to the six ports of the microfluidic device are also measured by the regulator through the same software [Fig. 9(b)], shown in great agreement with the previously computed values [Fig. 9(a)].

-
- [1] T. M. Squires and S. R. Quake, Microfluidics: Fluid physics at the nanoliter scale, *Rev. Mod. Phys.* **77**, 977 (2005).
- [2] G. M. Whitesides, The origins and the future of microfluidics, *Nature (London)* **442**, 368 (2006).
- [3] D. Mark, S. Haeblerle, G. Roth, F. von Stetten, and R. Zengerle, Microfluidic lab-on-a-chip platforms: requirements, characteristics and applications, *Chem. Soc. Rev.* **39**, 1153 (2010).
- [4] S. Battat, D. A. Weitz, and G. M. Whitesides, Nonlinear phenomena in microfluidics, *Chem. Rev.* **122**, 6921 (2022).
- [5] A. Manz, D. J. Harrison, E. M. J. Verpoorte, J. C. Fetters, A. Paulus, H. Lüdi, and H. M. Widmer, Planar chips technology for miniaturization and integration of separation techniques into monitoring systems, *J. Chromatogr. A* **593**, 253 (1992).
- [6] X. Mao, J. R. Waldeisen, and T. J. Huang, “Microfluidic drifting”—implementing three-dimensional hydrodynamic focusing with a single-layer planar microfluidic device, *Lab Chip* **7**, 1260 (2007).
- [7] K. Drescher, Y. Shen, B. L. Bassler, and H. A. Stone, Biofilm streamers cause catastrophic disruption of flow with consequences for environmental and medical systems, *Proc. Natl. Acad. Sci. USA* **110**, 4345 (2013).
- [8] P. Garstecki *et al.*, Formation of monodisperse bubbles in a microfluidic flow-focusing device, *Appl. Phys. Lett.* **85**, 2649 (2004).
- [9] E. Amstad, S. S. Datta, and D. A. Weitz, The microfluidic post-array device: high throughput production of single emulsion drops, *Lab Chip* **14**, 705 (2014).
- [10] T. T. Perkins, D. E. Smith, and S. Chu, Single polymer dynamics in an elongational flow, *Science* **276**, 2016 (1997).
- [11] A. Shenoy, C. V. Rao, and C. M. Schroeder, Stokes trap for multiplexed particle manipulation and assembly using fluidics, *Proc. Natl. Acad. Sci. USA* **113**, 3976 (2016).
- [12] G. V. Kaigala, R. D. Lovchik, and E. Delamarche, Microfluidics in the “open space” for performing localized chemistry on biological interfaces, *Angew. Chem. Int. Ed.* **51**, 11224 (2012).
- [13] K. C. Bhargava, B. Thompson, and N. Malmstadt, Discrete elements for 3D microfluidics, *Proc. Natl. Acad. Sci. USA* **111**, 15013 (2014).
- [14] A. K. Au, W. Huynh, L. F. Horowitz, and A. Folch, 3D-printed microfluidics, *Angew. Chem. Int. Ed.* **55**, 3862 (2016).
- [15] K. Takahashi, S. Kamiya, H. Takao, F. Shimokawa, and K. Terao, Stainless microfluidic probe with 2D-array microapertures, *AIP Adv.* **11**, 015331 (2021).
- [16] H. S. M. Coxeter, *Regular Polytopes*, 3rd ed. (Dover Publications, New York, 1973).
- [17] D. Gross, The role of symmetry in fundamental physics, *Proc. Natl. Acad. Sci. USA* **93**, 14256 (1996).
- [18] R. Zandi, D. Reguera, R. F. Bruinsma, W. M. Gelbart, and J. Rudnick, Origin of icosahedral symmetry in viruses, *Proc. Natl. Acad. Sci. USA* **101**, 15556 (2004).
- [19] E. M. Purcell, Life at low Reynolds number, *Am. J. Phys.* **45**, 3 (1977).
- [20] E. Lauga, and T. R. Powers, The hydrodynamics of swimming microorganisms, *Rep. Prog. Phys.* **72**, 096601 (2009).
- [21] A. P. Berke, L. Turner, H. C. Berg, and E. Lauga, Hydrodynamic attraction of swimming microorganisms by surfaces, *Phys. Rev. Lett.* **101**, 038102 (2008).
- [22] G. J. Elfring and E. Lauga, Hydrodynamic phase locking of swimming microorganisms, *Phys. Rev. Lett.* **103**, 088101 (2009).
- [23] P.-A. Goyette *et al.*, Microfluidic multipoles theory and applications, *Nat. Commun.* **10**, 1781 (2019).
- [24] J. Gonzalez and B. Liu, Symmetry-based nonperturbative micromanipulation in a three-dimensional microfluidic device, *Phys. Rev. Fluids* **5**, 044202 (2020).
- [25] W. Fang, T. Xiong, O. S. Pak, and L. Zhu, Data-driven intelligent manipulation of particles in microfluidics, *Adv. Sci.* **10**, 2205382 (2022).

- [26] A. Ashkin, J. M. Dziedzic, J. E. Bjorkholm, and S. Chu, Observation of a single-beam gradient force optical trap for dielectric particles, *Opt. Lett.* **11**, 288 (1986).
- [27] J. Wu, Acoustical tweezers, *J. Acoust. Soc. Am.* **89**, 2140 (1991).
- [28] D. G. Grier, Optical tweezers in colloid and interface science, *Curr. Opin. Colloid Interface Sci.* **2**, 264 (1997).
- [29] Q. Luan, C. Macaraniag, J. Zhou, and I. Papautsky, Microfluidic systems for hydrodynamic trapping of cells and clusters, *Biomicrofluidics* **14**, 031502 (2020).
- [30] M. Q. Tu, H. V. Nguyen, E. Foley, M. I. Jacobs, and C. M. Schroeder, 3D manipulation and dynamics of soft materials in 3D flows, *J. Rheology* **67**, 877 (2023).
- [31] A. Shenoy, D. Kumar, S. Hilgenfeldt, and C. M. Schroeder, Flow topology during multiplexed particle manipulation using a stokes trap, *Phys. Rev. Appl.* **12**, 054010 (2019).
- [32] The stress distribution is intrinsic to the far-field hyperbolic topology because any offset from the hyperbolic point, such as with a minimal planar extensional flow [38], is equivalent to adding a mean flow that imposes zero stress. For instance, taking that example flow velocity $\mathbf{v} \propto x\hat{x} - y\hat{y}$, the strain rate is found to be $\dot{\gamma} \propto \hat{x}\hat{x} - \hat{y}\hat{y}$. A displaced field, i.e., $\mathbf{v} \propto (x - a_x)\hat{x} - (y - a_y)\hat{y}$ for some physical displacement of the center (a_x, a_y) , is trivially seen to separate into the original field with an added mean flow, and the strain rate is identical and likewise invariant.
- [33] P. B. Pal, *A Physicist's Introduction to Algebraic Structures: Vector Spaces, Groups, Topological Spaces and More* (Cambridge University Press, Cambridge, United Kingdom, 2019).
- [34] A. J. M. Spencer, *Continuum Mechanics*, Longman Mathematical Texts (Longman, London, New York, 1980).
- [35] See Supplemental Material at <http://link.aps.org/supplemental/10.1103/PhysRevResearch.6.023234> for detailed information about movies.
- [36] K. Taute, S. Gude, S. Tans, and T. Shimizu, High-throughput 3D tracking of bacteria on a standard phase contrast microscope, *Nat. Commun.* **6**, 8776 (2015).
- [37] J. Gallian, *Contemporary Abstract Algebra*, 10th ed. (Chapman and Hall/CRC, Boca Raton, London, New York, 2021).
- [38] G. K. Batchelor, *An Introduction to Fluid Dynamics*, 2nd ed. (Cambridge University Press, Cambridge, United Kingdom, 2000).
- [39] P. J. Davis, *Circulant Matrices*, Pure and Applied Mathematics (Wiley, New York, 1979).